



Article

Parametric Investigation on the Electrical-Thermal Performance of Battery Modules with a Pumped Two-Phase Cooling System

Jun Wang ^{1,2} , Lin Ruan ^{1,2,*}  and Ruiwei Li ^{1,2}¹ Institute of Electrical Engineering Chinese Academy of Sciences, Beijing 100190, China² University of Chinese Academy of Sciences, Beijing 100049, China

* Correspondence: rosaline@mail.iee.ac.cn

Abstract: The pumped two-phase cooling method is a practical way to dissipate heat from the battery module. The operating parameters of the cooling system should be investigated thoroughly to improve the performance of the battery thermal management system (BTMS). However, the previous BTMS designs only explored the thermal performance and ignored the electrical performance in the battery module. This study designed a pumped two-phase cooling BTMS with the refrigerant of R1233zd. An electrothermal coupled model was established for a series-connected battery module to predict thermal and electrical behavior. The results showed that the pumped two-phase cooling system could obtain excellent cooling performance with low system pressure under 2C discharging condition. The average temperature of the module and the temperature difference among cells could be maintained under 40 °C and 5 K under a 2C discharging rate. A lower saturation temperature, higher mass flux, and higher subcooling degree could enhance heat dissipation for the cooling system based on R1233zd. An increase in the saturation temperature and a decrease in the subcooling degree could enhance the temperature uniformity within the module. The battery consistency was mainly dominated by the temperature difference and deteriorated with a lower average temperature in the pack. The research outcome of this paper can guide the design and optimization of the pumped two-phase cooling BTMS.

Keywords: battery thermal management; pumped two-phase cooling; electrothermal model; electrical-thermal performance



Citation: Wang, J.; Ruan, L.; Li, R. Parametric Investigation on the Electrical-Thermal Performance of Battery Modules with a Pumped Two-Phase Cooling System. *Energies* **2022**, *15*, 7897. <https://doi.org/10.3390/en15217897>

Academic Editors: Weifeng Li, Zhenhai Gao, Yupeng Chen, Yang Xiao and Yan Wang

Received: 14 September 2022

Accepted: 19 October 2022

Published: 25 October 2022

Publisher's Note: MDPI stays neutral with regard to jurisdictional claims in published maps and institutional affiliations.



Copyright: © 2022 by the authors. Licensee MDPI, Basel, Switzerland. This article is an open access article distributed under the terms and conditions of the Creative Commons Attribution (CC BY) license (<https://creativecommons.org/licenses/by/4.0/>).

1. Introduction

To reduce the emissions of greenhouse gases, the development of electric vehicles (EVs) has received increasing attention. The battery is one of the core segments of electric vehicles, and its performance has a direct impact on its safety, comfort, and economy. Lithium-ion batteries with strong power density, high energy density, high power density, and low self-discharge rate are widely applied in electric vehicles. Some new technologies, such as porous media [1,2], have been applied in lithium-ion batteries to obtain better performance. Despite all this, the performance of the lithium-ion cells may still be strongly restricted by the operating temperature. The operating temperature should be kept in the range of 25~40 °C to lengthen the cycle life and avoid thermal runaway [3]. Meanwhile, the temperature deviation within the battery pack can reduce the performance of the pack and accelerate the aging speed, which should be controlled within 5 °C [4,5]. Therefore, effective thermal management of the battery pack is essential to achieve high performance and long cycle life for lithium-ion batteries.

The battery thermal management methods can be divided into air cooling [6], liquid cooling [7], and phase-change cooling [8] by the cooling medium. Air cooling has advantages of complexity, cost, and weight. However, the poor thermal conductivity and small heat capacity of the air makes it only proper for HEVs with small-capacity battery packs, such as the Honda Insight and Toyota Prius [9]. The liquid cooling method has

been widely used in EVs due to its high cooling performance. However, the structure of a liquid cooling system is more complex, and the additional components make the cooling system more weight [10,11]. Additionally, the potential leakage problem should be avoided [12]. The phase change cooling method has gained more importance due to its excellent performance. The cell heat generation is absorbed by the phase change process, including the solid–liquid process and liquid–vapor process. The solid–liquid BTMSs have advantages in terms of lightness, high efficiency, and simplicity [13]. However, to address the problem of latent heat recovery, the heat conductivity of phase change materials needs to be enhanced urgently [14,15]. The liquid–vapor BTMSs can achieve better cooling performance compared to traditional liquid cooling under the same condition [16]. Among them, the direct evaporative cooling method and the pumped two-phase cooling method are the two representative methods of the liquid–vapor BTMSs [17,18].

The direct evaporative cooling BTMS contains an evaporator in the battery pack, which can be integrated with the air conditioning system of EVs directly. The evaporation process of the refrigerant is applied to absorb the battery heat generation. However, the operating pressure is up to 0.5 MPa of the direct evaporative cooling system, which has higher requirements for the pressure resistance and tightness performance of the pipe system [19]. In addition, the temperature uniformity may be deteriorated due to the superheat of the refrigerant at the end of the channel [16]. The pumped two-phase cooling BTMS is comprised of two circulation systems, including the pumped two-phase cooling BTMS and the air conditioning system. The chiller is used to exchange heat between the air conditioning system and the battery cooling system. Refrigerants with boiling point above 273.15 K under 1 atm, such as R1233zd and HFE-7000, are selected as a coolant in BTMS. So, the attractive advantages of pumped two-phase cooling BTMS include lower operating pressure and power consumption. The instable flow of the coolant can be prevented by controlling the pump speed. Additionally, the dryness of the refrigerant could be maintained at an optimum range even under high heat flux, which guarantees the temperature uniformity of the pack [20].

There have been some studies about the pumped two-phase cooling BTMS. Wang et al. [20] directly immersed the cells in refrigerant HFE-7000 and developed a novel direct flow boiling system. It was discovered that the temperature rise in the battery pack was dictated by the forced convection heat transfer. Additionally, the saturated boiling of the coolant and the local disturbance around cells enhanced the temperature uniformity effectively. The temperature difference among cells was kept within 3.71 K under 5C discharge. However, there were problems with this novelty method, such as higher cost and volume. Another widely cooling structure was through the cold plate contacting with the cell to remove heat. Choi et al. [21] proposed a cooling system using HFE-7000 as the coolant for a fuel cell application. It was demonstrated that the heat flux and vapor quality dominated the boiling heat transfer performance of the HFE-7000, but it was less sensitive to mass flux. Fang et al. [22] designed a pumped two-phase cooling system using the newly developed refrigerant R1233zd. The results showed that the average temperature of the dummy battery was significantly affected by the mass flux and vapor quality. An optimum value of vapor quality could be found to obtain the maximum cooling amount. The start-up and transient thermal performance of the pumped two-phase cooling system were investigated experimentally with different operating parameters in Ref. [23]. Experimental results showed that the transient performance could be adjusted by the flow rate and heat flux. The electrical performance during the boiling heat transfer process was seldom discussed in research. However, the above studies focus only on the thermal performance of the cooling system, and the thermal effects during the boiling heat transfer process on the electrical performance of the module were seldom discussed in research either. An et al. [18] utilized the phase change of the NOVEC-7000 in the mini-channel cold plate to absorb heat. The thermal performance and electrochemical performance of the battery pack were evaluated experimentally under various mass flow rates and discharge

rates. It was shown that the temperature uniformity and voltage distribution within the pack could be controlled in a desired range.

In summary, the pumped two-phase cooling BTMS is demonstrated to have excellent thermal performance. However, the existing discussions are mainly focused on the feasibility of its application. The research on the design and operation parameters of the pumped two-phase cooling BTMS is not adequate. It is important to discuss the operation parameters comprehensively, including mass flux, saturation temperature and subcooling degree. In addition, the above-mentioned works are mainly concentrated on the thermal performance of the BTMSs. The thermal effect on the electrical performance of the battery module in the pumped two-phase cooling system is still unknown, which has a significant influence on the aging rates of the pack. Meanwhile, a more accurate electrothermal coupled model for the pack with a two-phase cooling system is still lacking, which is important for the optimum design of the pack.

In this paper, a pumped two-phase cooling BTMS is designed with the refrigerant R1233zd. A comprehensive model for a 16 serially connected module is established comprising the electrical model and the fluid–solid coupling heat transfer model of the two-phase cooling BTMS. Thus, the temperature and voltage distribution in the module can be captured. The impacts of mass flux, saturation temperature and subcooling degree of the refrigerant on the thermal performance and electrical performance within a module are discussed in detail.

2. Model Development

A commonly used prismatic lithium-ion cell of 50 Ah is utilized in this research with NCM/Graphite electrodes, as shown in Figure 1a. The basic parameters of this battery are given in Table 1.

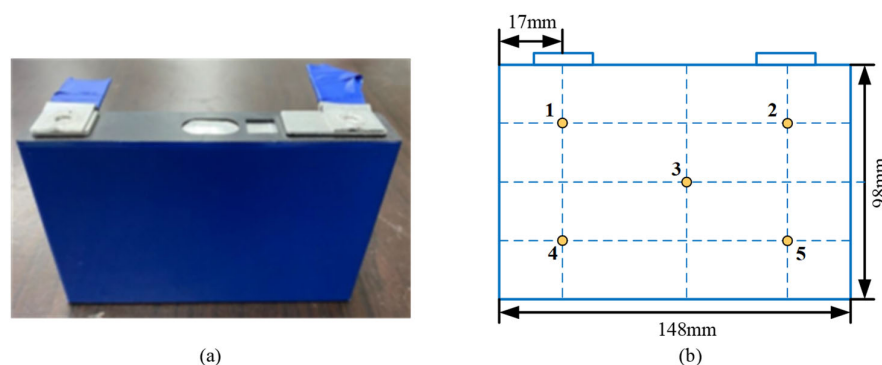


Figure 1. Prismatic lithium-ion battery. (a) Front view; (b) temperature monitoring points [24].

Table 1. Basic parameters of the battery.

Parameters	Value
Rated capacity	50 Ah
Rated voltage	3.65 V
Positive electrode	$\text{LiNi}_{0.6}\text{Co}_{0.2}\text{Mn}_{0.2}\text{O}_2$
Negative electrode	Graphite
Cut-off voltage at charge	4.25 V
Cut-off voltage at discharge	2.75 V

2.1. Electrothermal Model for Battery

An accurate electrical model and thermal model should be established for the cell to describe the dynamic electric and thermal behavior under different conditions. There are two main categories for battery electrical models. One is the electrochemical model, in which the electrochemical process inside the battery is described by a series of partial differential equations. The electrochemical models could provide more accurate simulation

results [25]. The other is the equivalent circuit model (ECM), which is established by simple electrical components [26]. The equivalent circuit models only need a few parameters and provide adequate accuracy. In this study, a second-order ECM has been established to define the prismatic battery. The model equation can be expressed as:

$$U_L = U_{OCV} - U_1 - U_2 - IR_0 \quad (1)$$

$$\dot{U}_1 = -\frac{U_1}{R_1 C_1} + \frac{I}{C_1} \quad (2)$$

$$\dot{U}_2 = -\frac{U_2}{R_2 C_2} + \frac{I}{C_2} \quad (3)$$

where U_{ocv} is the open circuit voltage of the cells, which is related to the state of charge (SOC). U_1 and U_2 are the terminal voltages of $R_1 C_1$ and $R_2 C_2$, respectively. R_0 is the internal ohmic resistance. R_1 and C_1 are the electrochemical polarization resistance and capacitance, respectively. R_2 and C_2 are the concentration polarization resistance and capacitance, respectively. $R_0, R_1, R_2, C_1,$ and C_2 are extracted from the HPPC tests under different SOC and temperature levels, which are realized into the equivalent circuit model as Look-Up Tables (LUTs).

Assume that the heat generation inside the cell is uniform and the heat generation in the tab is ignored. The temperature distribution in the cell follows the energy conversation laws, and is given by [27]:

$$\rho_{cell} C_{p,cell} \frac{dT}{dt} = K_{in} \left(\frac{\partial^2 T}{\partial x^2} + \frac{\partial^2 T}{\partial z^2} \right) + K_{th} \left(\frac{\partial^2 T}{\partial y^2} \right) + q_{cell} \quad (4)$$

where ρ_{cell} is the volume-average density, $C_{p,cell}$ is the volume-average specific heat capacity, T is temperature, K_{in} is the in-plane thermal conductivity of the prismatic battery, K_{th} is the through-plane thermal conductivity of the prismatic battery, and q_{cell} is the volume-average heat generation rate of the battery. To reduce the complexity of the model, the specific heat capacity $C_{p,cell}$ and density ρ_{cell} are assumed to be invariable [28]. The battery thermal capacity $\rho_{cell} C_{p,cell}$ is calculated by the volume of each part, as follows [29]:

$$\rho_{cell} C_{p,cell} = \frac{\sum \rho_i C_{p,i} V_i}{\sum V_i} \quad (5)$$

where V_i is the volume of each part in the cell. Considering the layered structure of prismatic cells, the thermal conductivity of the battery in in-plane and through-plane directions can be expressed as:

$$K_{in} = \frac{\sum K_i L_i}{\sum L_i} \quad (6)$$

$$K_{th} = \frac{\sum L_i}{\sum L_i / K_i} \quad (7)$$

The reduced heat generation formula proposed by Bernardi [30] is used for the battery:

$$q_{cell} = I(U_L - U_{ocv}) + IT_{cell} \frac{dU_{ocv}}{dT_{cell}} \quad (8)$$

where I is the operating current of the battery, U_{ocv} and U_L are the open circuit voltage and the terminal voltage of the battery, and T_{cell} is the volumetric temperature of the battery. dU_{ocv}/dT is the entropy coefficient, which is relevant to SOC [31]. In Equation (8), $I(U_L - U_{ocv})$ is the irreversible heat, and $ITdU_{ocv}/dT$ is the reversible heat.

The operating temperature affects the output electrical behavior by changing the electrical components parameters in ECM. The change in electrical components parameters affects the heat generation of the battery in turn, and then changes the battery temperature. In this study, the equivalent circuit model couples with the thermal model by the parameters

heat generation rate q and temperature T to obtain a more accurate electric and thermal behavior of the battery.

2.2. Electrothermal Model for Battery Pack

To satisfy the desired driving power and range, the battery pack for electrical vehicles always consists of large amounts of cells connected by series and parallel. As discussed in previous research, the performance of a single battery cannot represent the performance of the module or pack [4,32]. The small deviation of the internal structure of cells and the inconsistency of the operation condition inside the pack lead to the temperature non-uniformity within the pack. The non-uniform temperature in the pack may result in inconsistency in the aging rate, capacity, and electrical performance. Therefore, further research on the electrothermal coupling effect of the battery module is helpful to utilize it more effectively.

In this paper, a model of the battery module coupling the electrothermal model of cells, the fluid–solid coupling heat transfer model and the series-connected electrical model is established. Compared with previous works, the proposed model has the following advantages. Firstly, the model integrates a dynamic heat generation model for the cell level, instead of a constant heat source. Thus, the effects of realistic operating conditions on the performance of the module can be simulated. Secondly, the model integrates an electrical circuit model for the module level. Thus, the battery inconsistency caused by non-uniform temperature distribution within the module could be captured. The evolution of voltage distribution improves the prediction accuracy of the battery temperature in turn. The sub-models in different scales and domains and their parameters transfer relationship are shown in Figure 2; the detailed descriptions can be found below.

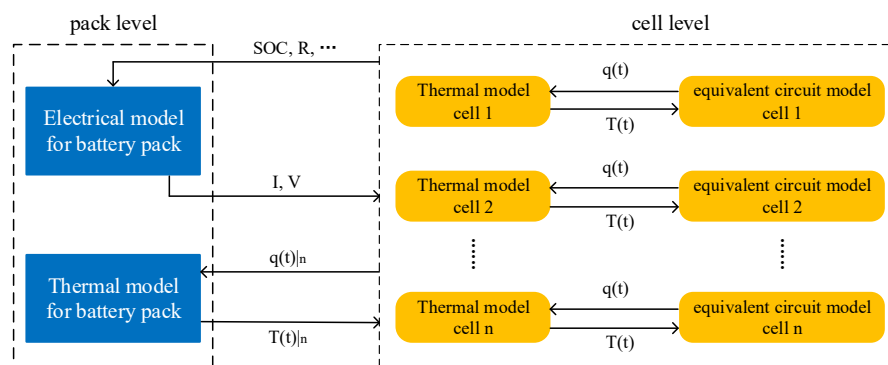


Figure 2. The coupling relationship of the electrothermal model for the battery pack.

2.2.1. Electrical Model for Battery Module

Assuming that all cells have the same internal structure and the connecting resistances between cells are ignored, an electrical model for the battery module including 16 cells connected in series has been built in the ANSYS Twinbuilder environment. The electrical model for the battery module is established by the ECM model of the single cell directly connected in series. Thus, the voltage distribution within the module could be captured by the electrical model.

For the series-connected battery module, the discharge voltage and current distribution for the module satisfy Equation (9).

$$\begin{aligned} V_{out} &= V_1 + V_2 + \dots + V_n \\ I_{out} &= I_1 = I_2 = \dots = I_n \end{aligned} \tag{9}$$

As discussed above, there are deviations in operation conditions among cells. The temperature distributions in the battery pack are inconsistent, which means that the operating temperatures of each cell are different. However, the electrical parameters of cells

depend on the operating temperature. For series-connected battery packs, the cells operate at the same current, but different voltages resulted from the non-uniform temperature distribution.

2.2.2. Thermal Model for Battery Module

As shown in Figure 3a, a common thermal management system structure for the battery pack is applied in this paper, in which the cold plate is underneath the battery module. Thin thermal pads are inserted between cells to improve the temperature uniformity in the module. The thermal pad is also set between the cold plate and the battery module to reduce the temperature difference. As shown in Figure 3b, the thickness of the cold plate is 15 mm, and an S-shaped flow channel with an inner diameter of 6 mm.

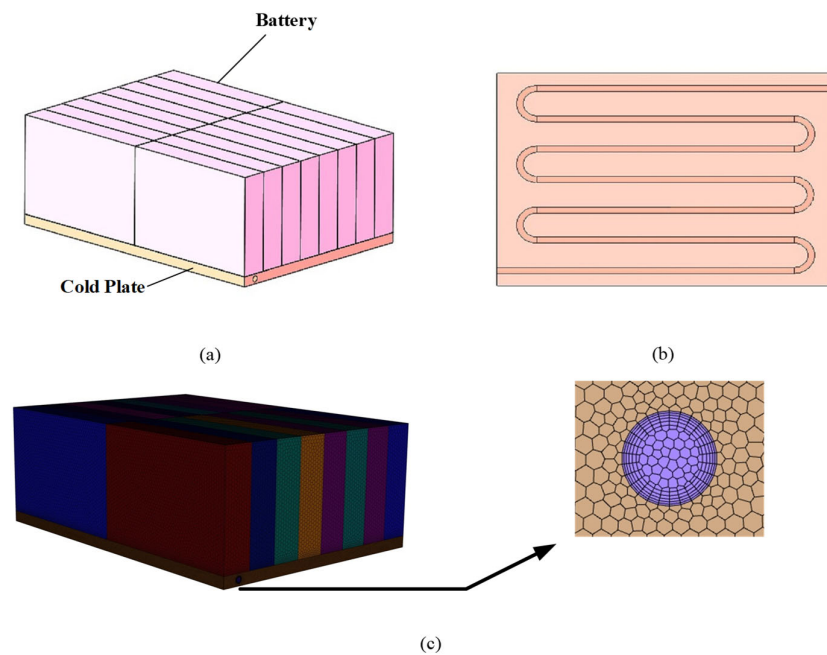


Figure 3. (a) Structure of the battery module with thermal management; (b) structure of the cold plate; (c) display of the grids.

- Solid domain

Equation (4) for a single cell can also be utilized to calculate the temperature distribution in the module. The thermal balance equations for the other solid domains are established by the same theory, including cold plates and thermal pads. The differences are that the equations do not consider the heat source term and the anisotropy of thermal conductivity. For example, the conversation equation in the cold plate can be expressed as Equation (10).

$$(\rho C_p)_{cp} \frac{\partial T_{cp}}{\partial t} = k_{cp} \left(\frac{\partial^2 T}{\partial x^2} + \frac{\partial^2 T}{\partial y^2} + \frac{\partial^2 T}{\partial z^2} \right) \quad (10)$$

The boundary conditions at the battery and cold plate interfaces and the wall of the S-shaped channel follows Newton's cooling law as defined in Equation (11).

$$\begin{aligned} -k_{in} \frac{\partial T}{\partial n} &= -k_{cp} \frac{\partial T}{\partial n} \\ -k_{cp} \frac{\partial T}{\partial n} &= h(T_w - T_l) \end{aligned} \quad (11)$$

where k_{in} , k_{cp} represent the thermal conductivity of the battery and the cold plate, respectively. h is the convective heat transfer coefficient. T_w , T_l are the temperature of the solid wall and fluid domain, respectively. The specific properties of solid domains in battery module are listed in Table 2.

Table 2. Structure and material parameters.

Parameter	Cell	Cold Plate	Thermal Pad
Density (kg/m ³)	2373	2689	3100
Specific heat capacity (J/(kg·K))	1120	951	930
Thermal conductivity (W/(m·K))	K _{in} = 40.8; K _{th} = 1.17	237.5	5
Specifications	148 mm × 98 mm × 26 mm	296 mm × 208 mm × 15 mm	296 mm × 208 mm × 2 mm

- Liquid domain

In this study, the R1233zd is selected as the coolant of the BTMS. Its saturation temperature is 17.9 °C under 101.325 kPa. The molecular weight is 130.5 g/mol. Assume that the material parameters of the refrigerant only dominated by the temperature, as shown in Table 3, which can be retrieved by software REFPROP 9.0 [33].

Table 3. R1233zd properties.

	Liquid Phase	Vapor Phase
Density (Kg·m ⁻³)	$3 \times 10^{-5}T^3 - 2.7 \times 10^{-2}T^2 + 6.56T + 998.94$	$2 \times 10^{-5}T^3 - 1.44 \times 10^{-2}T^2 + 3.56T - 299.84$
Specific heat capacity (J/Kg·°C)	$4 \times 10^{-4}T^3 - 3.78 \times 10^{-2}T^2 + 109.89T - 9480.6$	$5 \times 10^{-5}T^3 - 3.69 \times 10^{-2}T^2 + 11.154T - 501.85$
Thermal Conductivity (W/m·°C)	$-3 \times 10^{-9}T^3 + 3 \times 10^{-6}T^2 - 1.4 \times 10^{-3}T + 0.2828$	$1 \times 10^{-9}T^3 - 8 \times 10^{-7}T^2 + 3 \times 10^{-4}T - 0.0306$
Viscosity (Kg/m·s)	$-7 \times 10^{-10}T^3 + 7 \times 10^{-7}T^2 - 2 \times 10^{-4}T + 0.0265$	$3 \times 10^{-13}T^3 - 3 \times 10^{-10}T^2 + 1 \times 10^{-7}T - 8 \times 10^{-6}$

In this research, the transient VOF model in ANSYS FLUENT is applied to solve the complex heat and mass transfer process during phase change. Assume the flow of R1233zd is incompressible, so the density is invariable. The sum of volume fraction for the two-phase in per unit volume constantly is 1 [34]. Tracking of the interface between phases is determined by the continuity equation:

Liquid phase:

$$\frac{\partial \alpha_f}{\partial t} + \nabla \cdot (\alpha_f \vec{u}_f) = \frac{1}{\rho_f} \sum (\dot{m}_{gf} - \dot{m}_{fg}) \quad (12)$$

Vapor phase:

$$\frac{\partial \alpha_g}{\partial t} + \nabla \cdot (\alpha_g \vec{u}_g) = \frac{1}{\rho_g} \sum (\dot{m}_{fg} - \dot{m}_{gf}) \quad (13)$$

where α , \vec{u} , ρ and \dot{m} represent the volume fraction, velocity vector, density, and mass transfer rate, respectively. The indexes f and g represent liquid phase and vapor phase, respectively. \dot{m}_{gf} and \dot{m}_{fg} represent the mass transfer during phase change.

The momentum and energy equations are given by:

$$\frac{\partial}{\partial t}(\rho \vec{u}) + \nabla \cdot (\rho \vec{u} \vec{u}) = -\nabla P + \nabla \cdot \left[\mu \left(\nabla \vec{u} + \nabla \vec{u}^T \right) \right] + \vec{F} \quad (14)$$

and

$$\frac{\partial}{\partial t}(\rho E) + \nabla \cdot (\vec{u}(\rho E + P)) = \nabla \cdot [k_{eff} \nabla T] + S_h \quad (15)$$

where E (J/kg) is energy per mass; μ , ρ and k_{eff} are dynamic viscosity, density, and effective thermal conductivity. The properties of fluid are calculated by:

$$\phi = \sum \alpha_i \phi_i \quad (16)$$

where ϕ is the property being determined by the volume fraction of per phase in the control volume. Implicit body force formulation is used to describe the detachment of vapor and replenishment of liquid into the near-wall region. The Continuum Surface Force (CSF)

method proposed by Brackbill is used to model the surface tension force \vec{F} with wall adhesion [35].

The source term S_h in the energy equation, which describes the extra energy involved in phase change, can be expressed as:

$$S_h = \dot{m}h_{fg} \quad (17)$$

where h_{fg} (J/kg) is the latent heat.

Using an applicable phase change model is crucial for capturing the heat and mass transfer in phase change accurately. In this research, the Lee model is selected for solving the mass transfer rates of R1233zd, which is given by:

$$\dot{m}_{fg} = r_i \alpha_f \rho_f \frac{(T_f - T_{sat})}{T_{sat}} \text{ for evaporation } (T_f > T_{sat}) \quad (18)$$

and

$$\dot{m}_{gf} = r_i \alpha_g \rho_g \frac{(T_{sat} - T_g)}{T_{sat}} \text{ for condensation } (T_g < T_{sat}) \quad (19)$$

where r_i is an empirical coefficient representing mass transfer intensity. The value of r_i has a profound impact on the interface temperature. The appropriate value of r_i can be determined by several calculations [36]. In this research, $r_i = 1$ was selected to make the interface temperature close to the saturation temperature. The Renormalization Group (RNG) $k - \varepsilon$ turbulence model and scalable wall function were applied to account for the turbulence effects. The governing equations of RNG $k - \varepsilon$ are expressed as:

$$\begin{aligned} \frac{\partial k}{\partial t} + U_j \frac{\partial k}{\partial x_j} &= -\overline{u_i u_j} \frac{\partial U_i}{\partial x_j} + \frac{\partial}{\partial x_j} \left(\frac{K_m}{\sigma_k} \frac{\partial k}{\partial x_j} \right) - \varepsilon \\ \frac{\partial \varepsilon}{\partial t} + U_j \frac{\partial \varepsilon}{\partial x_j} &= -C_{\varepsilon 1} \frac{\varepsilon}{k} \overline{u_i u_j} \frac{\partial U_i}{\partial x_j} + \frac{\partial}{\partial x_j} \left(\frac{K_m}{\sigma_\varepsilon} \frac{\partial \varepsilon}{\partial x_j} \right) - C_{\varepsilon 2} \frac{\varepsilon^2}{k} - R \end{aligned} \quad (20)$$

where k and ε are the turbulent kinetic and the turbulent dissipation rate, respectively. σ_k , σ_ε , $C_{\varepsilon 1}$ and $C_{\varepsilon 2}$ are the empirical constants. K_m is the turbulent viscosities of momentum. The pressure-outlet boundary condition was applied at the outlet of the channel to avoid any outlet effects.

The finite-volume method is adopted in FLUENT to solve the engineering problem. The computational domain is meshed into a number of elements. As shown in Figure 3c, a poly-hexcore grid was applied to mesh the 3D model. The boundary layer grid was used in the near-wall region of the channel to improve the wall treatment. The size of elements in a certain domain has a significant impact on the accuracy of calculated results. For transient simulation, a smaller time step will reduce the simulation efficiency and a larger time step may cause convergence difficulty. As a result, grid independence and time-step independence testing should be conducted to choose the appropriate grid size and time step before computation.

The volume-average temperature of the battery module was utilized to demonstrate the grid independence and time-step independence. The grid number is 70 w, 100 w, 142 w, 200 w, and 300 w, respectively. The time-step number includes 5, 10, 20, 40, 80, and 100 steps·s⁻¹. As shown in Figure 4a, the relative deviation of the volume-average temperature of battery module between 200 w cells and 300 w cells was 0.01 K, which meant the calculation results were independent of the grid number. As shown in Figure 4b, the change range of the volume-average temperature of the battery module was rather small when the time-step number was larger than 20 steps·s⁻¹. With the independence validations, the time-step number was selected as 20 steps·s⁻¹ and the BTM model was meshed into 200 w to balance the calculation accuracy and efficiency.

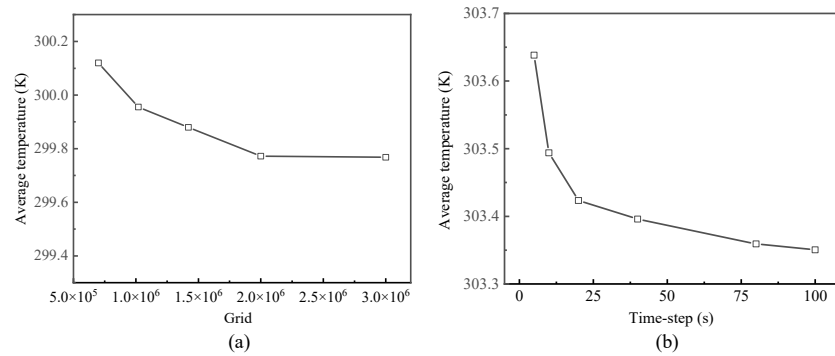


Figure 4. (a) Grid independence validation; (b) time-step independence validation.

3. Model Validation

- Electrothermal model

The electrothermal coupled model for a single cell was built in ANSYS environment to simulate a battery electric and thermal behaviors. The specific parameters of the prismatic battery are given in Table 2. The electrical and thermal behaviors under 1C discharge at 20 °C ambient temperature in Ref. [24] were used to validate the accuracy of the electrothermal coupled model. The average temperature of the battery was calculated by the five temperature test points shown in Figure 1b. The errors between the simulation and the experiment for battery voltage and temperature were less than 5%, which indicated the simulation results were consistent with the experiment results, as shown in Figure 5a,b.

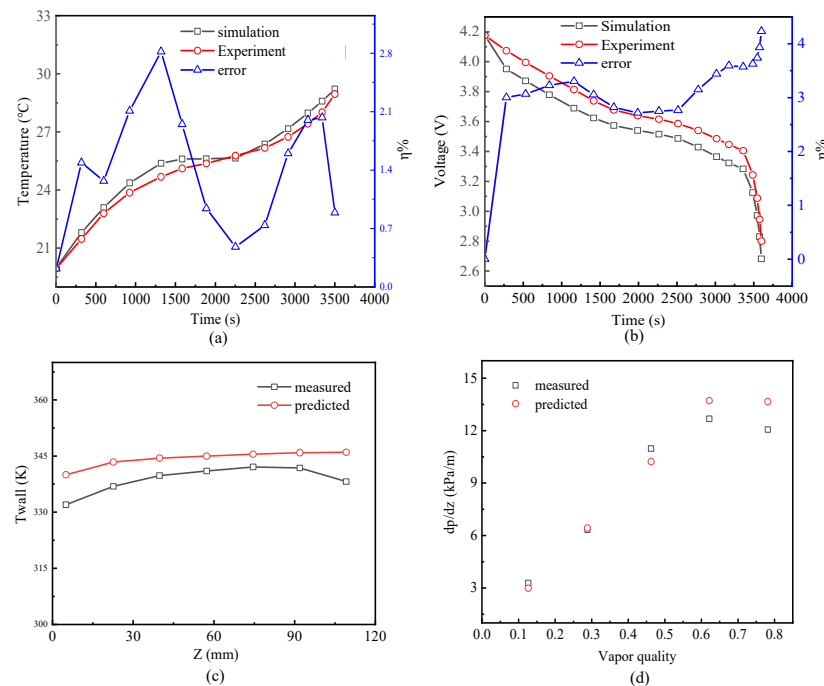


Figure 5. Model verification (a) surface temperature of the cell; (b) terminal voltage of the cell; (c) wall temperature distribution; (d) pressure drop gradient.

- VOF model

To validate the accuracy of the temperature distribution simulated by the VOF model, experiment results in Ref. [37] were used in this research. The experiment explored the subcooled flow boiling of the FC-72 in a rectangular channel. The inlet mass flux of the refrigerant was 445.75 kg/m²s. The saturation temperature was 333.31 K. The heat flux was 143 kw/m². As shown in Figure 5c, the calculated wall temperature distribution under

the same condition were compared with the experimental data in Ref. [37]. The maximum over-prediction was about 7 K compared to the measurements, which showed that the simulation values were in good agreement with the experimental results.

The pressure gradient of refrigerant HFC-134a in a straight adiabatic circular tube was studied in the experiment in Ref. [38], and the experimental results were compared with the simulated pressure drop in this research. The refrigerant mass flux was $301 \text{ kg/m}^2\text{s}$ and the evaporative temperature of the refrigerant was $5.8 \text{ }^\circ\text{C}$. The pressure gradients from the simulation and experimental results were compared at different vapor quality and shown to have good agreement in Figure 5d. The numerical method can thus extend to simulate the temperature distribution within the module and the subcooled flow boiling performance in the cold plate.

4. Results and Discussion

4.1. Performance of the Pumped Two-Phase Cooling System

In this section, the saturation temperature, mass flux and subcooling degree were set as 295.15 K, $1238 \text{ kg/m}^2\text{s}$ and 4 K, respectively to qualitative study the cooling performance of the pumped two-phase cooling BTMS. The temperature field of the module at 600 s was shown in Figure 6a. The temperature was increased along the flow direction due to the decrease in the temperature difference between coolant and battery. This trend could be reflected in temperature distribution of cold plate, as shown in Figure 6b. Meanwhile, an obvious temperature gradient could be observed in the height direction. This was unavoidable when the cold plate was placed underneath the battery module. The temperature of R1233zd in the channel was shown in Figure 6c. The temperature at the inlet was 291.15 K. The refrigerant temperature gradually rose when it flowed along the channel, reaching about 297.4 K at the outlet. As shown in Figure 6d, the vapor volume fraction was zero at the entrance region. The single-phase convection heat transfer dominated the cooling process in this region. Then, the vapor volume fraction was higher than zero when the refrigerant temperature reached the local saturation temperature, which indicated that the evaporation process appeared. The nucleate boiling heat transfer dominated the cooling process in this region. According to Figure 6b, the temperature gradient in the single-phase convection heat transfer region was significantly higher than that in the nucleate boiling heat transfer region. This showed the superiority of nucleate boiling in terms of temperature uniformity.

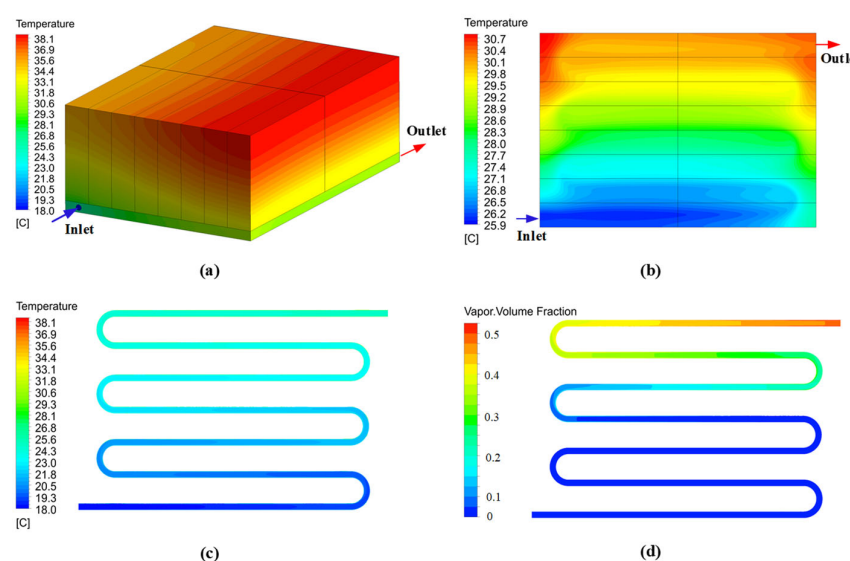


Figure 6. (a) temperature field of the module; (b) temperature field of cold plate; (c) temperature of R1233zd; (d) vapor volume fraction in channel.

4.2. Parametric Study

The cooling performance of the pumped two-phase cooling BTMS can be varied by controlling the saturation temperature, mass flux, and subcooling degree through the cooling power of the condenser and pump speed. To improve the performance of the pumped two-phase cooling BTMS, the effects of saturation temperature, subcooling degree, and mass flux on the BTMS should be discussed in detail. The simulation conditions were given in Table 4. Here, the average temperature of the module, the maximum temperature difference among cells, and the battery consistency were used as analysis indexes to quantify the cooling performance of the BTMS.

Table 4. Simulation condition of R1233zd property.

No.	Saturation Temperature (K)	Subcooling Degree (K)	Mass Flux (kg/m ² s)	Discharge Rate (C)	Ambient Temperature (K)
1	291.15/293.15/295.15/297.15	4	1238	2	313.15
2	291.15	2/3/4/5	1238	2	313.15
3	291.15	4	742.8/990.4/1238/1485.6	2	313.15

4.2.1. Saturation Temperature

The saturation temperature of refrigerant is a function of the saturation pressure, which can be adjusted by the cooling power of the condenser [16,39]. In this study, the pressure at the outlet of the S-shaped channel in the cold plate is considered as the saturation pressure of R1233zd, which is 100.13 kPa corresponding to the saturation temperature of 291.15 K in the initial setting. The saturation temperature was set to 291.15 K (100.13 kPa), 293.15 K (107.96 kPa), 295.15 K (116.27 kPa), 297.15 K (125.06 kPa), respectively, to investigate the effect of the saturation temperature on the performance of the pumped two-phase cooling BTMS.

Figure 7 shows the cooling performance of the pumped two-phase cooling BTMS according to the saturation temperature. As shown in Figure 7a, the heat dissipation was enhanced as the saturation temperature decreased. As the saturation temperature of the R1233zd decreased, the average temperature of the battery module at 600 s dropped from 309.0 K to 305.6 K. Meanwhile, the average temperature of the module dropped much faster with a lower saturation temperature. The average temperature decrease rate increased from 0.41 K/min to 0.75 K/min, when the evaporating temperature of the R1233zd decreased from 297.15 K to 291.15 K. These results are consistent with the research studies [27,28,40]. The temperature difference between the module and the refrigerant increased when the saturation temperature of the R1233zd decreased, which was the intrinsic cause for the enhancement of cooling capacity.

The temperature non-uniformity of the module was strengthened with the saturation temperature decreased. Figure 7b shows that the maximum temperature difference of the module at 600 s increased from 3.01 K to 3.55 K when the evaporating temperature decreased from 297.15 K to 291.15 K, which showed a different trend to the average temperature of the module. The temperature difference among cells mainly depends on the temperature variation of the refrigerant along the flow direction, which is the result of the combined effects of pressure drop for the flow resistance, the temperature increase due to the absorption of sensible heat, and the influence of the increase in the dryness on the cooling capacity. The temperature difference of the refrigerant along the channel was smaller when the saturation temperature increased, which resulted in more uniform temperature distribution in the module.

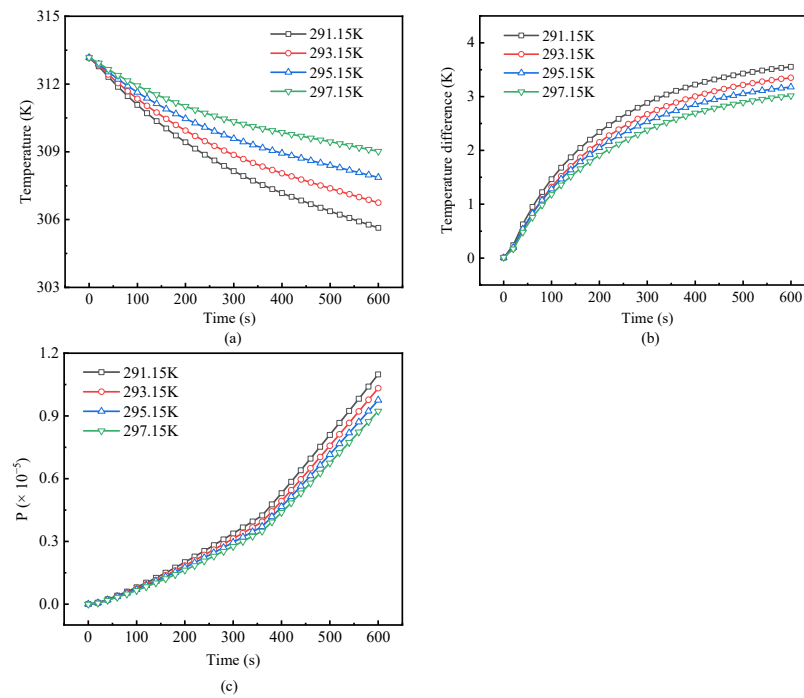


Figure 7. The effects of saturation temperature (a) Average temperature of the module; (b) Temperature uniformity of the module; (c) Battery consistency in the module.

Figure 7c shows the influence of the saturation temperature on the battery consistency. The normalized battery consistency index P of the module is defined as [41]:

$$P = \frac{1}{|U_n^{ae}|} \sqrt{\frac{1}{N-1} \sum_{n=1}^N (U_n^e - U_n^{ae})^2} \quad (21)$$

$$U_n^e = \frac{u_n}{e_n} \quad (22)$$

$$U_n^{ae} = \frac{1}{N} \sum_{n=1}^N U_n^e \quad (23)$$

where N is the number of cells in the module, u_n is the operating voltage, e_n is the rated voltage, U_n^e is the normalized voltage given by Equation (21), and U_n^{ae} is the average normalized voltage of the module expressed by Equation (22). The closer the P is to zero, the better the consistency of the module during the discharge. As presented in Figure 7c, the battery consistency of the module increased as the saturation temperature of the refrigerant increased, which showed a similar trend to the temperature difference. The corresponding temperature difference among the series-connected cells leads to higher internal resistance of cells with lower temperature. The series-connected cells have same operating currents; the output voltage of colder cells with higher internal resistance drops more significantly, resulting in the non-uniformity of terminal voltage in the module. As discussed in previous research [32], the temperature difference among cells is positively correlated with the battery inconsistency of the module. It was noteworthy that the change rate of P increased over time. As discussed in Ref. [42], the battery consistency of the module is dominated by the temperature difference among cells and the average temperature of the module. The lower average temperature and worse temperature uniformity of the module over time aggravates the battery inconsistency of the module. Therefore, the slope of P increased over time.

4.2.2. Mass Flux

In a pumped two-phase cooling system, the speed of the mechanical pump could control the mass flux of the R1233zd entering the cold plate. The mass flux was set to 742.8 kg/m²s, 990.4 kg/m²s, 1238 kg/m²s, and 1485.6 kg/m²s, respectively, to explore its effects on the performance of the module.

Figure 8a shows the average temperature of the module under different mass flux. The cooling capacity was improved as the mass flux increased. The average temperature of the module decreased from 309.2 K to 304.4 K as the mass flux increased from 742.8 kg/m²s to 1485.6 kg/m²s. Meanwhile, the average temperature of the module dropped much faster with a higher mass flux. The average temperature decrease rate increased from 0.39 K/min to 0.87 K/min when the mass flux increased. The cooling performance intensifies with a higher mass flux due to acceleration of the process of bubbles from generation to departure, which enhances the boiling heat transfer. However, with the mass flux continuing to increase, the average temperature of the module decreased more gently, which indicated that the cooling performance improvement was increasingly minor. Similar phenomenon could be found in Ref. [28]; the average temperature of the battery pack dropped slightly after the mass flow rate of the refrigerant reached a certain value. Therefore, the strategy to improve the cooling amount by increasing the mass flux of the refrigerant was effective only within a limited range. There exists an ideal mass flux to balance the cooling performance and energy consumption.

As shown in Figure 8b, there was no linear relationship between temperature uniformity and mass flux. The temperature difference increased with the mass flux when it was lower than 1238 kg/m²s. As shown in Figure 8c, the value of P also increased as the mass flux increased in this range, indicating that the battery consistency worsened. The increasing temperature difference resulted in increasing unbalanced discharging. However, when the mass flux exceeded 1238 kg/m²s, the temperature difference decreased. In this range, the average temperature of the module reduced slightly with increasing mass flux, indicating that the improvement in the cooling amount was minor. Further increasing the mass flux had a more considerable effect on the reduction in the temperature of the hotter batteries. Meanwhile, the heat generation of colder batteries was higher than that of the hotter batteries due to the higher internal resistance. Therefore, the temperature uniformity of the battery module improved. The value of P also decreased in this range, as shown in Figure 8c, due to the enhancement of the temperature uniformity within the battery module. In the stage of slight change in the average temperature of the module, the battery consistency within the battery module was dominated by the temperature difference among cells as the mass flux continued to increase.

To guarantee the system efficiency, increasing the mass flux was usually not recommended in the pumped two-phase cooling system when reaching the limited improvement of the cooling amount. However, the temperature uniformity and battery consistency could be enhanced by increasing the mass flux of the refrigerant in this stage.

4.2.3. Subcooling Degree

The subcooling degree at the inlet of the channel is comprehensively affected by the cooling power in the condenser and the mass flux of the refrigerant, which affects the cooling performance of the system by controlling the area of nucleate boiling heat transfer. In this research, the subcooling degree was set to 2 K, 3 K, 4 K, and 5 K, respectively, to explore its effects on the performance of the module.

Figure 9a shows the average temperature of the module under different subcooling degrees. It can be seen that an increase in the subcooling degree led to better cooling capacity. The average temperature of the module decreased by 1.67 K as the subcooling degree increased from 2 K to 5 K. Meanwhile, the average temperature decrease change rate of the battery module was 0.64 K/min and 0.81 K/min when the subcooling degree was 2 K and 5 K, respectively, which meant that the cooling capacity increased by nearly 1.3 times. The heat absorption of the refrigerant is the sum of the sensible heat and latent heat. The

volume fraction of vapor phase at the outlet of the channel was almost the same as the subcooling degree increased from 2 K to 5 K, which indicated that the latent heat ingested by the refrigerant under various subcooling degree in the simulation range was almost the same. The higher the subcooling degree, the higher the heat of the battery module that can be absorbed by the sensible heat of the refrigerant, which showed a higher cooling capacity.

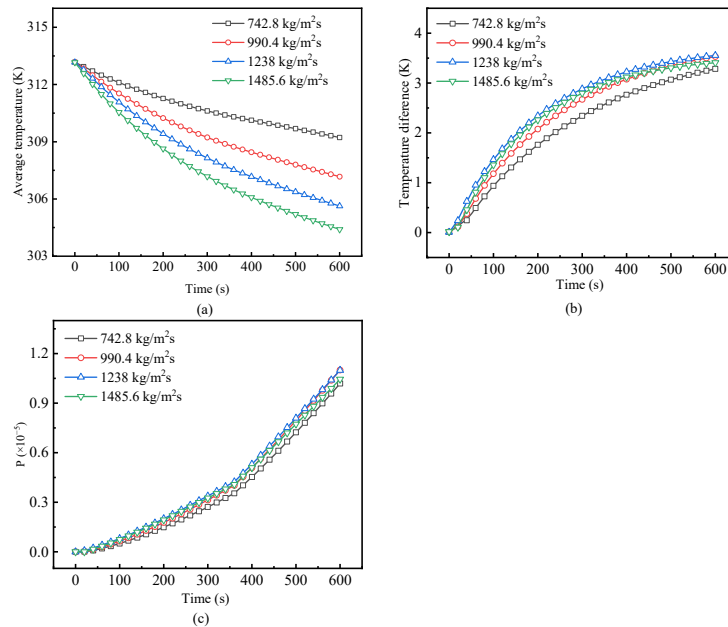


Figure 8. The effects of mass flux. (a) Average temperature of the module; (b) Temperature uniformity of the module; (c) Battery consistency in the module.

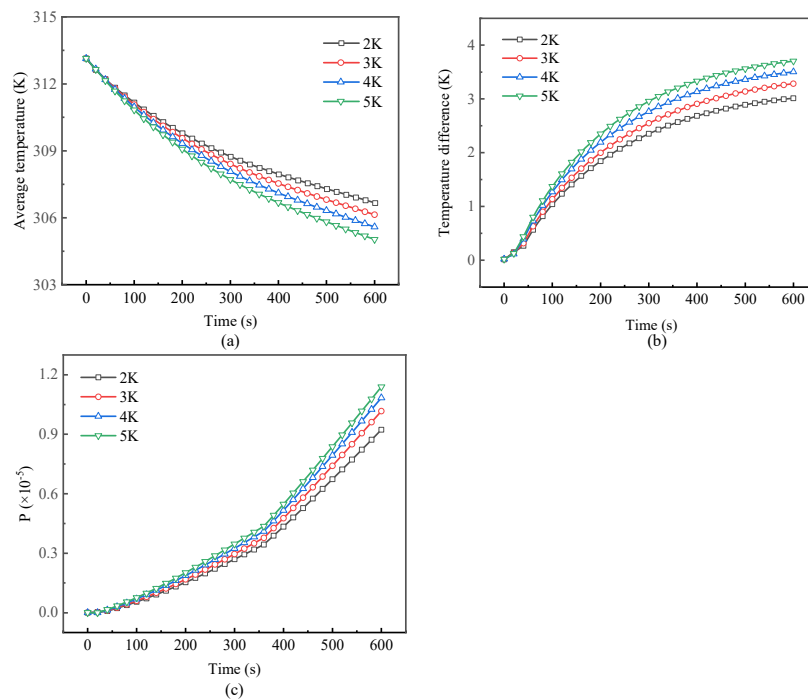


Figure 9. The effects of subcooling degree. (a) Average temperature of the module; (b) Temperature uniformity of the module; (c) Battery consistency in the module.

As shown in Figure 9b, the temperature uniformity of the module worsened as the subcooling degree increased. The temperature difference increased from 3.0 K to 3.7 K as the

subcooling degree at the inlet of the cold plate increased from 2 K to 5 K. The evaporating temperature of the refrigerant did not change in this simulation condition, which meant that the temperature of the refrigerant R1233zd at the outlet of the channel with different subcooling degree was almost the same. Therefore, the temperature variation in the R1233zd along the channel increased as the subcooling degree increased. As discussed in Section 4.1, the increasing temperature difference of the refrigerant along the flow direction resulted in worse temperature uniformity in the module. The value of P also increased as the subcooling degree increased due to the deterioration in the temperature uniformity within the battery module.

5. Conclusions

In this study, an electrothermal coupled model in ANSYS environment was established for the battery module with BTMS based on R-1233zd flow boiling. The average temperature of the module, the maximum temperature difference among cells, and the battery consistency were used as analysis criteria to evaluate the cooling performance of the newly proposed BTMS under different saturation temperature, mass flux, and subcooling degree. Several conclusions can be addressed here:

- (1) The pumped two-phase cooling BTMS could obtain excellent cooling performance with lower system pressure compared with the direct cooling system due to the use of the low-pressure refrigerant R1233zd. The average temperature of the module and the temperature difference among cells could be maintained under 40 °C and 5 K under a 2C discharging rate.
- (2) A lower saturation temperature, higher mass flux, and higher subcooling degree of the refrigerant enhanced the heat transfer between the module and the refrigerant, thus achieving lower average temperature and a higher temperature decrease rate in the battery module. An increase in the saturation temperature and decrease in the subcooling degree could reduce the temperature difference within the module. However, the mass flux of the refrigerant showed a two-stage effect on the temperature uniformity in the module. The results shows that the cooling performance of the BTMS could be improved by controlling the above three operation parameters.
- (3) The battery consistency in the module was mainly dominated by the temperature uniformity in the pack, and showed a positive relationship with it. Meanwhile, the battery consistency deteriorated with a lower average temperature.

In the future, we propose that the following progresses should be subject to further research:

- (1) The aging model should be integrated into the electrothermal model to further investigate the effects of operation parameters on the aging performance.
- (2) More realistic cyclic conditions should be tested to validate the effectiveness of the pumped two-phase cooling BTMS.
- (3) The optimum design of cooling structure for the pumped two-phase cooling BTMS should be paid more attention to achieve better cooling performance.

Author Contributions: J.W.: Conceptualization; Data curation; Formal analysis; Investigation; Writing—original draft; Methodology. L.R.: Funding acquisition; Project administration; Writing—Review and Editing. R.L.: Writing—Review and Editing. All authors have read and agreed to the published version of the manuscript.

Funding: This research received no external funding.

Conflicts of Interest: The authors declare no conflict of interest.

Nomenclature

C_p	Specific heat capacity (J/(kg·K))
E	Energy per unit mass (J/kg)
e_n	Rated voltage (V)
\vec{F}	Surface tension force (N)
h	Convective heat transfer coefficient (W/(m ² ·K))
I	Current (A)
k	Turbulent kinetic energy (m ² s ⁻²)
K_{in}	In-plane thermal conductivity of the cell (W/(m·K))
K_{th}	Through-plane thermal conductivity of the cell (W/(m·K))
K_{cp}	Thermal conductivity of cold plate (W/(m·K))
k_{eff}	Effective thermal conductivity of fluid (W/(m·K))
K_m	Turbulent viscosities of momentum
\dot{m}	Mass transfer rate
L	Length (m)
P	Battery consistency
q	Heat generation (W)
R	Resistance of cell
S_h	Extra energy involved in phase change (J)
T	Temperature (K)
T_w	Temperature of solid wall (K)
T_l	Temperature of fluid (K)
U_{ocv}	Open circuit voltage of the cell (V)
U_L	Terminal voltage of the cell (V)
\vec{u}	Velocity vector
u_n	Operating voltage (V)
U_n^e	Normalized voltage
U_n^{ae}	Average normalized voltage
V	Volume (m ³), voltage (V)
Greek letters	
α	Volume fraction
ε	Turbulent dissipation rate (m ² s ⁻³)
μ	Dynamic viscosity (Kg/m ² ·s)
ρ	Density (kg m ⁻³)
ϕ	Fluid property
Subscripts and superscript	
f	Liquid phase
g	Vapor phase
i	Number of cell parts
n	Number of cells
Abbreviation	
BTMS	Battery Thermal Management System
CSF	Continuum Surface Force
EV	Electric Vehicle
ECM	Equivalent Circuit Model
LUT	Look-Up Table
RNG	Renormalization Group
SOC	State Of Charge

References

1. Xiao, B.; Wang, W.; Zhang, X.; Long, G.; Fan, J.; Chen, H.; Deng, L. A novel fractal solution for permeability and Kozeny-Carman constant of fibrous porous media made up of solid particles and porous fibers. *Powder Technol.* **2019**, *349*, 92–98. [\[CrossRef\]](#)
2. Liang, M.; Fu, C.; Xiao, B.; Luo, L.; Wang, Z. A fractal study for the effective electrolyte diffusion through charged porous media. *Int. J. Heat Mass Transf.* **2019**, *137*, 365–371. [\[CrossRef\]](#)
3. Baghdadi, I.; Briat, O.; Delétage, J.Y.; Gyan, P.; Vinassa, J.M. Lithium battery aging model based on Dakin's degradation approach. *J. Power Sources* **2016**, *325*, 273–285. [\[CrossRef\]](#)

4. Paul, S.; Diegelmann, C.; Kabza, H.; Tillmetz, W. Analysis of ageing inhomogeneities in lithium-ion battery systems. *J. Power Sources* **2013**, *239*, 642–650. [[CrossRef](#)]
5. Liu, H.; Wei, Z.; He, W.; Zhao, J. Thermal issues about Li-ion batteries and recent progress in battery thermal management systems: A review. *Energy Convers. Manag.* **2017**, *150*, 304–330. [[CrossRef](#)]
6. Ashwin, T.R.; MCGordon, A.; Jennings, P.A. Electrochemical modelling of Li-ion battery pack with constant voltage cycling. *J. Power Sources* **2017**, *341*, 327–339. [[CrossRef](#)]
7. Chen, S.; Peng, X.; Bao, N.; Garg, A. A comprehensive analysis and optimization process for an integrated liquid cooling plate for a prismatic lithium-ion battery module. *Appl. Therm. Eng.* **2019**, *156*, 324–339. [[CrossRef](#)]
8. Huo, Y.; Rao, Z. Investigation of phase change material based battery thermal management at cold temperature using lattice Boltzmann method. *Energy Convers. Manag.* **2017**, *133*, 204–215. [[CrossRef](#)]
9. Kelly, K.J.; Mihalic, M.; Zolot, M. Battery usage and thermal performance of the Toyota Prius and Honda Insight during chassis dynamometer testing. In Proceeding of the IEEE 2002 Battery Conference on Applications & Advances, Long Beach, CA, USA, 18 January 2002.
10. Huang, Y.; Wang, S.; Lu, Y.; Huang, R.; Yu, X. Study on a liquid cooling-based battery thermal management system considering transient regime pertaining. *Appl. Therm. Eng.* **2020**, *16*, 114394.
11. Yang, W.; Zhou, F.; Liu, Y.; Xu, S.; Chen, X. Thermal performance of honeycomb-like battery thermal management system with bionic liquid mini-channel and phase change materials for cylindrical lithium-ion battery. *Appl. Therm. Eng.* **2021**, *188*, 116649. [[CrossRef](#)]
12. Lai, Y.; Wu, W.; Chen, K.; Wang, S.; Xin, C. A compact and lightweight liquid-cooled thermal management solution for cylindrical lithium-ion power battery pack. *Int. J. Heat Mass Transf.* **2019**, *144*, 118581. [[CrossRef](#)]
13. Chen, F.; Huang, R.; Wang, C.; Yu, X.; Liu, H.; Wu, Q.; Qian, K.; Bhagat, R. Air and PCM cooling for battery thermal management considering battery cycle life. *Appl. Therm. Eng.* **2020**, *173*, 115154. [[CrossRef](#)]
14. Samimi, F.; Babapoor, A.; Azizi, M.; Karimi, G. Thermal management analysis of a Li-ion battery cell using phase change material loaded with carbon fibers. *Energy* **2016**, *96*, 355–371. [[CrossRef](#)]
15. Babapoor, A.; Azizi, M.; Karimi, G. Thermal management of a Li-ion battery using carbon fiber-PCM composites. *Appl. Therm. Eng.* **2015**, *82*, 281–290. [[CrossRef](#)]
16. Hong, S.H.; Jang, D.S.; Park, S.; Yun, S.; Kim, Y. Thermal performance of direct two-phase refrigerant cooling for lithium-ion batteries in electric vehicles. *Appl. Therm. Eng.* **2020**, *173*, 115213. [[CrossRef](#)]
17. Cen, J.; Li, Z.; Jiang, F. Experimental investigation on using the electric vehicle air conditioning system for lithium-ion battery thermal management. *Energy Sustain. Dev.* **2018**, *45*, 88–95. [[CrossRef](#)]
18. An, Z.; Jia, L.; Li, X.; Ding, Y. Experimental investigation on lithium-ion battery thermal management based on flow boiling in mini-channel. *Appl. Therm. Eng.* **2017**, *117*, 534–543. [[CrossRef](#)]
19. Guo, J.; Jiang, F. A novel electric vehicle thermal management system based on cooling and heating of batteries by refrigerant. *Energy Convers. Manag.* **2021**, *237*, 14145. [[CrossRef](#)]
20. Wang, Y.F.; Wu, J.T. Thermal performance predictions for an HFE-7000 direct flow boiling cooled battery thermal management system for electric vehicles. *Energy Convers. Manag.* **2020**, *207*, 112569. [[CrossRef](#)]
21. Choi, E.J.; Jin, Y.P.; Min, S.K. Two-phase cooling using HFE-7100 for polymer electrolyte membrane fuel cell application. *Appl. Therm. Eng.* **2018**, *148*, 868–877. [[CrossRef](#)]
22. Fang, Y.; Ye, F.; Zhu, Y.; Li, K.; Shen, J.; Su, L. Experimental investigation on system performances and transient response of a pumped two-phase battery cooling system using R123zd. *Energy Rep.* **2020**, *6*, 238–247. [[CrossRef](#)]
23. Zhu, Y.; Fang, Y.; Su, L.; Ye, F. Experimental investigation of start-up and transient thermal performance of pumped two-phase battery thermal management system. *Int. J. Energy Res.* **2020**, *44*, 11372–11384. [[CrossRef](#)]
24. Xie, Y.; Zheng, J.; Hu, X.; Lin, X.; Liu, K.; Sun, J.; Zhang, Y.; Dan, D.; Xi, D.; Feng, F. An improved resistance-based thermal model for prismatic lithium-ion battery charging. *Appl. Therm. Eng.* **2020**, *180*, 115794. [[CrossRef](#)]
25. Kenney, B.; Darcovich, K.; MacNeil, D.D.; Davidson, I.J. Modelling the impact of variations in electrode manufacturing on lithium-ion battery modules. *J. Power Sources* **2012**, *213*, 391–401. [[CrossRef](#)]
26. Hosseinzadeh, E.; Arias, S.; Krishna, M.; Worwood, D.; Barai, A.; Widanalage, D.; Marco, J. Quantifying cell-to-cell variations of a parallel battery module for different pack configurations. *Appl. Energy* **2021**, *282*, 115859. [[CrossRef](#)]
27. Park, S.; Jang, D.S.; Lee, D.; Hong, S.H.; Kim, Y. Simulation on cooling performance characteristics of a refrigerant-cooled active thermal management system for lithium ion batteries. *Int. J. Heat Mass Transf.* **2019**, *135*, 131–141. [[CrossRef](#)]
28. Shen, M.; Gao, Q. Structure design and effect analysis on refrigerant cooling enhancement of battery thermal management system for electric vehicles. *J. Energy Storage* **2020**, *32*, 101940. [[CrossRef](#)]
29. Chen, S.C.; Wan, C.C.; Wang, Y.Y. Thermal analysis of lithium-ion batteries. *J. Power Sources* **2005**, *140*, 111–124. [[CrossRef](#)]
30. Bernardi, D.; Pawlikowski, E.; Newman, J. A General Energy Balance for Battery Systems. *J. Electrochem. Soc.* **1985**, *132*, 5. [[CrossRef](#)]
31. Forgez, C.; Do, D.V.; Friedrich, G.; Morcrette, M.; Delacourt, C. Thermal modeling of a cylindrical LiFePO₄/graphite lithium-ion battery. *J. Power Sources* **2010**, *195*, 2961–2968. [[CrossRef](#)]
32. Yang, N.; Zhang, X.; Shang, B.; Li, G. Unbalanced discharging and aging due to temperature differences among the cells in a lithium-ion battery pack with parallel combination. *J. Power Sources* **2016**, *306*, 733–741. [[CrossRef](#)]

33. Lemmon, E.W.; Huber, M.L.; McLinden, M.O. *REFPROP9.0*; NIST: Boulder, CO, USA, 2010.
34. *ANSYS FLUENT Theory Guide*; ANSYS Inc.: Canonsburg, PA, USA, 2009.
35. Brackbill, J.U.; Kothe, D.B.; Zemach, C. A continuum method for modeling surface tension. *J. Comput. Phys.* **1992**, *100*, 335–354. [[CrossRef](#)]
36. Qiu, G.D.; Cai, W.H.; Wu, Z.Y.; Jiang, Y.; Yao, Y. Analysis on the value of coefficient of mass transfer with phase change in Lee's equation. *J. Harbin Inst. Technol.* **2014**, *46*, 15–19.
37. Lee, J.; O'Neill, L.E.; Lee, S.; Mudawar, I. Experimental and computational investigation on two-phase flow and heat transfer of highly subcooled flow boiling in vertical upflow. *Int. J. Heat Mass Transf.* **2019**, *136*, 1199–1216. [[CrossRef](#)]
38. De Rossi, F.; Mauro, A.W.; Rosato, A. Local heat transfer coefficients and pressure gradients for R-134a during flow boiling at temperatures between $-9\text{ }^{\circ}\text{C}$ and $+20\text{ }^{\circ}\text{C}$. *Energy Convers. Manag.* **2009**, *50*, 1714–1721. [[CrossRef](#)]
39. Van Gils, R.W.; Danilov, D.; Notten, P.H.; Speetjens, M.F.; Nijmeijer, H. Battery thermal management by boiling heat-transfer. *Energy Convers. Manag.* **2014**, *79*, 9–17. [[CrossRef](#)]
40. Wang, Z.; Wang, Y.; Xie, Z.; Li, H.; Peng, W. Parametric investigation on the performance of a direct evaporative cooling battery thermal management system. *Int. J. Heat Mass Transf.* **2022**, *189*, 122685. [[CrossRef](#)]
41. Ding, C.; Wen, H. The influence of connection mode on the consistency and heat production of battery modules. *J. Beijing Univ. Aeronaut. Astronaut.* **2022**, *48*, 171–181. [[CrossRef](#)]
42. Liang, J.; Gan, Y.; Tan, M.; Li, Y. Multilayer electrochemical-thermal coupled modeling of unbalanced discharging in a serially connected lithium-ion battery module. *Energy.* **2020**, *209*, 118429. [[CrossRef](#)]